

# Improvement of the open circuit voltage by modifying the transparent ITO front electrode in amorphous n-i-p solar cells

F.-J. Haug<sup>\*1</sup>, R. Biron<sup>1</sup>, G. Kratzer<sup>1</sup>, F. Leresche<sup>1</sup>, J. Besuchet<sup>1</sup>, C. Ballif<sup>1</sup>, M. Dissel<sup>2</sup>, S. Kretschmer<sup>2</sup>, W. Soppe<sup>2</sup>, P. Lippens<sup>3</sup>, and K. Leitner<sup>3</sup>

<sup>1</sup> Ecole Polytechnique Fédérale de Lausanne (EPFL), Institute of Microengineering (IMT), Photovoltaics and Thin Film Electronics Laboratory, Rue A.-L. Breguet, 2000 Neuchâtel, Switzerland

<sup>2</sup> ECN, Solar Energy, P.O. Box 1, 1755 ZG Petten, The Netherlands

<sup>3</sup> Umicore, Thin Film Products AG, Alte Landstrasse 8, FL-9496 Balzers, Liechtenstein

Abstract:

At the front contact of thin film silicon solar cells, the junction between the p-doped window layer and the n-type transparent electrode results in a barrier that must be surmounted by the charge carriers. The barrier height is governed by the work function difference of these two materials. For different compositions of the well known  $\text{In}_2\text{O}_3\text{-SnO}_2$  (ITO) system, we find that higher oxygen partial pressure during sputter deposition increases the work function of the deposited films. Over the same range of oxygen partial pressures, ITO electrodes with low tin content applied to n-i-p type thin film silicon solar yield a gain in  $V_{oc}$  by up to 40 mV.

---

\* Corresponding author, e-mail: [franz-josef.haug@epfl.ch](mailto:franz-josef.haug@epfl.ch), phone: +41 32 718 3325

## Introduction

Photovoltaics is considered as one of the key ingredients in the sustainable energy mix of the future. Among the different technologies, thin film silicon is attractive for a variety of reasons; active layers with thickness of a few micrometers or less require only small amounts of an overall abundant material. The properties of thin film silicon have been well investigated during more than three decades of R&D in solar modules and flat panel displays, resulting also in a solid technology base for low cost production [1, 2]. Moreover, thin film silicon modules show favourable out-door performance. Single junction devices have demonstrated efficiencies exceeding 10% [3]. From a technological point of view, thin film silicon offers also a variety of combinations for high efficiency devices based on tandem or multi-junction devices. In purely amorphous cells, the high-gap of amorphous silicon can be combined with low-gap silicon-germanium alloys [4, 5]. Potential issues because of the scarce element germanium can be avoided by the combination with low gap cells of microcrystalline silicon [6] into micromorph tandems devices [7-9].

Thin film silicon solar cells are commonly distinguished in terms of their deposition sequence which is either of the p-i-n or the n-i-p type. Regardless of the type, charge transport properties require illumination through the p-layer, p-i-n cells are thus applied to rigid glass substrates. The n-i-p configuration shown in Figure 1 is suitable for opaque low cost substrates like stainless steel foils, but is also commonly used for polymer sheets. The unbreakable nature and the flexibility associated with these substrate types make the n-i-p configuration particularly attractive for consumer products and building integration.

In n-i-p cells, the material of choice for the transparent front contact is ITO, acronym for indium-tin-oxide which is almost always fabricated by sputter deposition from  $\text{In}_2\text{O}_3:\text{SnO}_2$  targets with varying ratio. ITO is an n-type semiconductor with a band-gap of more than 3.6 eV which makes it transparent for the visible and near UV spectrum. Typically, sputtering is carried out from ceramic targets which are slightly oxygen deficient for better conductivity and mechanical stability; thus, sputtering is carried out in Ar/O<sub>2</sub> mixtures. Insufficient oxidation yields conductive films with poor transparency because of a too metallic character of the layers. On the other hand, oversupply of oxygen yields transparent films with low conductivity because oxygen vacancies act as donors in ITO and because Sn dopants become inactive by incorporation as SnO<sub>2</sub> [10]. In films with high carrier density, free carrier absorption and reflection take place in the near or mid IR [11]. Consequently, for solar cell applications one aims at improving the mobility rather than high carrier density [12]. High conductivity is nevertheless mandatory because the thickness of ITO must typically be chosen between 65 and 70 nm in order to establish an antireflection condition at about 550 nm with the silicon absorber layer [13].

The upper panel of Figure 2 illustrates the band diagram of an idealized p-i-n junction based on amorphous silicon with electron affinity of 3.9 eV [14] and a band gap of 1.85 - 1.9 eV. In complete devices, the n-layer is electrically connected to the metal back contact or an n-type ZnO buffer layer; the behaviour of this junction is close to Ohmic and does not pose problems in general. Assuming a typical activation energy of 400 meV in the p-layer, a work function of about 5.4 eV would be required in the front contact in order to form an Ohmic contact between the p-layer and the front electrode. Recently, layers of high work-function metals consisting of nm sized particles before coalescence into continuous films have been reported to yield Ohmic contacts [15], but the control of the layer thickness may turn out to be difficult in large area applications. For ITO, the work function values in the literature scatter widely; Park reported a work function between 4.4 and 4.5 eV for ITO with In/Sn  $\approx$  6 [16], Minami found rather constant values between 4.8 and 4.9 eV for the whole composition range of  $\text{In}_2\text{O}_3 - \text{SnO}_2$  [17]. Klein applied photoelectron spectroscopy to pure  $\text{In}_2\text{O}_3$  films obtained by reactive evaporation with different oxygen partial pressures; with increasing oxygen pressure, the work

function varied from 4.3 to 4.7 eV [18]. The oxygen-rich films of this series were discussed in a separate study by Lang; for carrier densities ranging from  $2.2 \times 10^{-19}$  to  $7 \times 10^{-19} \text{ cm}^{-3}$ , corresponding to resistivities between  $6 \times 10^{-3}$  to  $2.5 \times 10^{-3} \text{ } \Omega\text{cm}$ , the band gap increases from 3.55 to 3.8 eV because of the Burstein-Moss shift [19]. Gassenbauer applied photoelectron spectroscopy to ITO films grown by RF sputtering in Ar/O<sub>2</sub> atmosphere from a 90/10 target; with increasing oxygen content in the plasma, the resistivity increased from  $2 \times 10^{-4}$  to  $5 \times 10^{-2} \text{ } \Omega\text{cm}$ , the work function increased from 4.6 to 5.2 eV [20]. These photoelectron studies find that the Fermi level should be located within the band gap which is explained by a surface layer with different stoichiometry [18, 20]. This idea is supported by various surface treatments which have been reported to change the work function; Sugiyama reported 4.3 eV for films exposed to oxygen depleting Ar-plasma, 4.5 eV for films with carbon impurities, and 4.8 eV after ozone treatment (measured on material with In/Sn  $\approx$  9) [21]. Similarly, variations in a range of 0.8 eV were reported for varying oxygen or argon treatments by Lee [22] and by Mason [23].

Most of the values quoted from the literature are below the requirement of for Ohmic contacts, and the details of interface chemistry for ITO films sputtered onto the p-layer are not known. The band diagram in Figure 2 uses therefore a representative of 4.8 eV from Minami's work and does not take into account surface depletion of ITO; the front contact in the solar cell consists thus of a Schottky junction with barrier height of about 0.6 eV [24, 25]. Current transport over the barrier proceeds either via thermionic emission, tunnelling, or tunnelling assisted emission. Except for pure tunnelling, the emission processes result in a reduction of the maximum achievable built-in-voltage, and therefore also a reduced open circuit voltage  $V_{oc}$ . Moreover, a wide barrier is expected to incur an additional series resistance.

In real solar cells, these considerations are further complicated; owing to the high defect density in doped layers, charge carriers that are generated in these layers are only poorly collected. This loss is particularly strong at the front of the device where light with short wavelengths is strongly absorbed. Therefore, state-of-the-art devices often use p-layers of high band-gap materials like silicon carbide [26] or silicon oxide [27]. Still, the p-layer must be kept as thin as possible, ideally between 10 and 20 nm. However, this makes the p-layer thinner than the space charge region of the junction between ITO and the p-layer which is roughly between 20 and 30 nm as estimated from the barrier height given above and a doping concentration of about  $10^{18} \text{ cm}^{-3}$  which emerges from typical values of doping efficiency and precursor gas ratio. Different from the scenario illustrated in Figure 2 b) where the p-layer is thick enough for the band bending to flatten out before the junction to the i-layer, Figure 2 c) illustrates thus the case of a more realistic device where the i-layer is connected to the curved part of a thin p-layer, resulting in a significantly reduced built-in-voltage.

In this contribution, we investigate ITO films with different composition. Their work function increases with reduced Sn-content and with the oxygen partial pressure during sputter deposition. The ITO films are also incorporated as front contact in n-i-p amorphous silicon solar cells with a double p-layer structure using microcrystalline silicon at the interface to ITO. Modelling results suggest that this configuration is compatible with low work function materials and shows a moderate gain with high work function; our experimental work confirms this prediction.

## Experimental

ITO films were deposited by sputtering at room temperature (planar magnetron with diameter of 104 mm, AJA Inc.) from ceramic targets (Umicore) of varying composition. The magnetrons are mounted in two lab type sputtering systems at ECN and EPFL, using a configuration that is designed for co-sputtering from up to four targets onto a rotating substrate holder. The design is intended for versatility and thickness uniformity rather than high deposition rates. Continuous DC excitation between 150 and 200 W was employed (at ECN: Advanced Energy, Pinnacle Plus, pulsing disabled; at EPFL: Maris,

ADL GmbH). Gas mixtures of 0, 0.5, 1.0, 1.5 and 2.5% of oxygen in argon were used at pressures between 0.3 (ECN) and 0.5 Pa (EPFL). All depositions were carried out at room temperature. The work function variation was measured at ECN directly after deposition. Samples were kept in dry atmosphere during the short transfer from the deposition system to the work function setup (KP Technology), an ex-situ version of the setup described in ref. [28]. Before each measurement, the setup was calibrated with gold and aluminium standards; the measurement of the standards is repeated after each measurement to detect possible drift. After the work function measurement, the resistivity was measured; subsequently the samples were subjected to 90 minutes annealing at 180°C in air, then their resistivity was measured again. Because shipping between the sites would have exposed the samples to non-reproducible conditions, the work functions were measured only on the ITO samples made at ECN.

At EPFL, ITO layers were fabricated under similar conditions and characterized optically (Lambda900, Perkin Elmer) and electrically (HMS 5000, Microworld). Moreover, they were incorporated into amorphous silicon solar cells using an n-i-p configuration on glass substrates coated with a flat rear reflector consisting of Ag-ZnO (120 + 60 nm). The silicon deposition was carried out at 190°C by plasma enhanced chemical vapour deposition (PE-CVD); details of the deposition process can be found in ref. [29]. We used a double p-layer configuration where the contact to the ITO is established by microcrystalline silicon because of its better doping efficiency [30]. After deposition of the ITO front contact, the cells were subjected to annealing for 90 minutes at 180°C in air which helps to recover sputter damage [31]. After annealing, the solar cells were measured under simulated AM1.5g illumination at 25°C.

## Results and discussion

### *Work function of ITO films*

Because the chemical potential (or Fermi-level) in semiconductors depends on doping, the work function is expected to change with the carrier density. In an n-type degenerate semiconductor with carrier concentration  $n$ , the Fermi-level resides within the conduction band and its actual position is governed by two competing effects; the Burstein-Moss shift describes the filling of states at the band edge which moves the highest occupied levels into the band. Not taking into account the additional effect of non-parabolic bands, the shift is proportional to  $n^{2/3}$  [32, 33]. At the same time, the overlapping wave functions of ever more closely spaced doping levels eventually merge with the conduction band edge, thus effectively reducing the electronic gap of forbidden states; the gap narrowing is proportional to  $n^{1/3}$  [34]. In ZnO and ITO, the combination of both effects is dominated by the upwards shift of the Fermi level [35, 36]. Overall, an increasing carrier density is therefore expected to reduce the work function, but it can additionally change with modifications of the surface chemistry and with adsorbates like carbon impurities [21]. Figure 3 shows experimentally determined work functions of samples from three different target compositions deposited in the ECN setup at 0.3 Pa in dependence of the oxygen partial pressure in the sputtering plasma. As general trend, it is observed that higher oxygen content in the plasma yields higher work function. Likewise, among the different ITO compositions lower SnO<sub>2</sub> content is reflected also by higher functions.

Owing to the fact that the ITO films deposited at the two sites are not comparable, and that the situation shown in Figure 1 is still a simplification of the actual experimental configuration, we used the modelling software ASA [37] for assessing the combination of different p-layer configurations with an ITO work function variation between 4.9 and 5.2 eV. The main modelling parameters are summarized in Table 1. The p-layer is assumed consist of a 10 nm thick double layer, taking into account the transition from a fully amorphous nucleation layer, p1, at the i-p interface into a microcrystalline layer, p2, towards the p-ITO interface. Figure 4 illustrates various combinations of p1

and p2. In reality, the thickness of the microcrystalline layer will fluctuate laterally because nucleation takes place spontaneously, resulting in various parallel Schottky junctions. Effectively, such a configuration will be dominated by the lowest Schottky barrier [38], i.e. between microcrystalline material and ITO, but the recombination properties in such a junction would require a more involved analysis than the employed 1D model.

From Figure 4 it is observed that the  $V_{oc}$  of cells with purely amorphous p-layer (10/0) relates almost linearly to the ITO work function whereas the double layers are increasingly insensitive to the work function of the front contact. Indeed, the use of a microcrystalline layer was reported to improve the contact resistance to ZnO:Al [39] whose work function was reported to be as low as 4.5 eV [17].

### ***Electrical properties of ITO films***

Figure 5 shows the resistivity of films deposited by continuous DC excitation; in their as-deposited state, all films show a more or less pronounced minimum for oxygen contents between 0.5 and 1.5%. Annealing reduces the resistivity in most films deposited with low oxygen content while the resistivity goes up consistently for those deposited with high oxygen flow. The corresponding Hall data are shown in Figure 6; all compositions show a trend of decreasing carrier density with oxygen content, the overall highest carrier densities are found in the 80/20 samples. After annealing, the carrier density increases for all Sn-rich compositions when the films are grown with low oxygen content, pointing towards activation of Sn dopants; however, the changes become relatively small towards the condition of optimum resistivity from Figure 5; on 97/3 samples the trend is less clear due to data scattering and 100/0 films degrade over the whole range. Towards higher oxygen content; the 80/20 samples show reduced carrier densities while the other increase again slightly. After annealing, the mobilities improve in all 80/20 samples, while they are generally decreased in the other compositions, excepting the region of low oxygen content which appears to behave inconsistently within the scatter. We note from Figure 6 that conditions of low oxygen partial pressure and high SnO<sub>2</sub> content generally yield films with high carrier density; Figure 3 shows films deposited under these conditions show reduced work function, thus corroborating the relation to the Fermi-level position that was briefly discussed in the previous section.

Figure 7 plots the mobilities of all shown samples against their carrier densities. The figure includes curves which describe the limiting behaviour for scattering at ionized impurity with single and double charge, taking additionally into account the dependence of the effective mass on carrier density in heavily degenerate semiconductors [40]. Except for low carrier densities, most of the samples with low SnO<sub>2</sub> content are close to the curve given by singly charged impurities ( $Z=1$ ), while the 80/20 samples are closer to trend of  $Z=2$ . Upon annealing, all samples approach the curve of doubly charged impurities. Within the SnO<sub>2</sub> variation, there are roughly three regimes; the 80/20 samples remain among the highest carrier densities, the 90/10 and 95/5 samples loose mobility but tend to keep their carrier density while the 97/3 and 100/0 exhibit a drop of both quantities. Figure 7 includes an additional characteristic which takes into account scattering at grain boundaries [40]; up to its intersection with the characteristic of singly charged impurities, this line appears to separate the initial from the annealed state for all of the ITO samples with low SnO<sub>2</sub> content.

For films deposited at room temperature, changes in resistivity are generally attributed to crystallisation of initially amorphous films [41]. Improved transport through the crystalline phase can yield lower resistivity, at the same time a reduction of the carrier density by annealing of donor-type oxygen vacancies may increase the resistivity. We can therefore attribute the overall decrease of carrier density with oxygen content in the sputtering plasma to a loss of the donor type oxygen vacancies, either by oxidation from the ambient air or due to activation of oxygen that is trapped in the films during deposition. For the samples with low SnO<sub>2</sub> content, annealing appears to add an additional

mobility limitation by grain boundary scattering. This is pronounced by their relatively low carrier density which yields wide depletion zones at the grain boundaries that are difficult to tunnel through.

### **Optical properties**

Figure 8 shows typical absorption data of 60 nm thick ITO films on glass. Films sputtered from the 95/5 target on glass are shown as representative example, the other target compositions show similar trends. Generally, the samples sputtered with low oxygen content show strong absorption even in the visible range of wavelengths. This is to some extent ameliorated by annealing, but the amount of transmission required for solar cell operation is only obtained for oxygen content higher than 1%. An additional effect of annealing is the blue-shift of the band gap absorption from typically 380 nm down to 350 nm, as well as increased IR absorption that is visible on all but the 0.5% sample. The optical effects of annealing are related to the changes in carrier density shown in Figure 6; in most samples, the carrier density increases and thus the frequency of reflection and absorption by the free carrier plasma is shifted from the IR towards the visible. Additionally, the Burstein-Moss effect widens the optical band gap in degenerate semiconductors. The loss in mobility is not directly visible in the optical data but it contributes to a broadening of the free carrier absorption.

### **Open circuit voltage**

The trends in open circuit voltage with respect to the oxygen content during sputtering of the different ITO compositions are shown in Figure 9. Up to four substrates with n-i-p solar cells from a co-deposition on flat Ag/ZnO reflector were finished with ITO front contacts from a given target composition, but using different oxygen partial pressures. Per substrate, the Voc of several cells is shown for statistics. The target compositions with low SnO<sub>2</sub> content, i.e. 90/10, 95/5, and 97/3 show a gain in Voc with increasing oxygen content. Across these three compositions, reduced SnO<sub>2</sub> content also yields a slight Voc increase. Overall, the gain is relatively moderate between 30 and 40 mV. Among these samples with low SnO<sub>2</sub> content, the behaviour is consistent with the notion that lower carrier density, either by more oxygen or by less Sn-doping, results in a higher work function which in turn yields higher Voc. However, the cells processed with the 80/20 target exhibit completely opposite behaviour; they show among the highest Voc values of all measured samples despite the fact that the high carrier density of the 80/20 films should yield the lowest work functions. Additionally, the dependence on oxygen partial pressure is also inverted. The origin of these observations is not clear at present, but may be related to the poorly understood interfacial stoichiometry of ITO. A possible explanation for the Voc decrease with increasing oxygen partial pressure which is observed for the 80/20 samples, may be related to increased sputter damage by negative oxygen ions which would give rise to more recombination and thus lower Voc. Recently, Ellmer showed that Sn targets yield enhanced amounts of negative oxygen ions compared targets made from pure In as well as from In-Sn alloys [42]. However, these observations were made during reactive sputtering from metallic targets, it is not clear whether they translate to ceramic targets and whether they would already appear within the much smaller composition range of our study.

### **Conclusions**

We investigated ITO films deposited by DC sputtering from targets with different In<sub>2</sub>O<sub>3</sub>-SnO<sub>2</sub> compositions. With increasing oxygen content in the Ar/O<sub>2</sub> plasma, the films undergo a transition from low resistivity and high absorption towards films with high resistivity and low absorption. At the same time, the work function is found to increase by approximately 150 mV. The ITO films have been incorporated as front contact into n-i-p type solar cells; in films with moderate SnO<sub>2</sub> content up to 10%, the variation of the work function results in enhanced open circuit voltage because the Schottky

barrier at the interface between the p-layer and the ITO front electrode is reduced. However ITO sputtered from a target with 20% SnO<sub>2</sub> showed a different behaviour whose understanding necessitates further experiments.

## **Acknowledgements**

We thankfully acknowledge funding by the European Union within the FP7 project Silicon-Light (contract No. 241277).

## References

- [1] M. Fecioru-Morariu, B. Mereu, J. Kalas, J. Hoetzel, P.A. Losio, M. Kupich, O. Kluth, T. Eisenhammer, 5th World PVSEC, Valencia, 2010, p. 2947.
- [2] S. Klein, S. Wieder, K. Buschbaum, K. Shchwanitz, T. Stolley, D. Severin, P. Obermeyer, M. Kress, E. Sommer, T. Marschner, M. Martini, S. Noll-Baumann, J. Haack, U.I. Schmidt, A. Straub, K. Ahmed, K. Schuegraf, 5 World PVSEC, Valencia, 2010, p. 2708.
- [3] S. Benagli, D. Borrello, E. Vallat-Sauvain, J. Meier, U. Kroll, J. Hoetzel, J. Bailat, J. Steinhäuser, M. Marmelo, G. Monteduro, L. Castens, 24th European PVSEC, Hamburg, 2009, p. 3BO.9.3.
- [4] J. Yang, A. Banerjee, S. Guha, *Applied Physics Letters* 70/22 (1997), p. 2975.
- [5] Y. Ichikawa, T. Yoshida, T. Hama, H. Sakai, K. Harashima, *Solar Energy Materials and Solar Cells* 66/1-4 (2001), p. 107.
- [6] J. Meier, R. Flückiger, H. Keppner, A. Shah, *Applied Physics Letters* 65/7 (1994), p. 860.
- [7] K. Yamamoto, A. Nakajima, M. Yoshimi, T. Sawada, S. Fukuda, T. Suezaki, M. Ichikawa, Y. Koi, M. Goto, T. Meguro, *Solar Energy* 77/6 (2004), p. 939.
- [8] J. Bailat, L. Fesquet, J.B. Orhan, Y. Djerdidane, B. Wolf, P. Madlinger, J. Steinhäuser, S. Benagli, D. Borrello, L. Castens, G. Monteduro, M. Marmelo, B. Dehbozorgi, E. Vallat-Sauvain, X. Multone, D. Romang, J.F. Boucher, J. Meier, U. Kroll, M. Despeisse, G. Bugnon, C. Ballif, S. Marjanovic, G. Kohnke, N. Borelli, K. Koch, J. Liu, R. Modavis, D. Thelen, S. Vallon, A. Zakharian, D. Weidmann, 5th World PVSEC, Valencia, 2010, p. 2720.
- [9] B. Yan, G. Yue, X. Xu, J. Yang, S. Guha, *physica status solidi (a)* 207/3 (2010), p. 671.
- [10] T. Minami, *MRS Bulletin* 25/8 (2000), p. 38.
- [11] I. Hamberg, C.G. Granqvist, *Journal of Applied Physics* 60/11 (1986), p. R123.
- [12] T. Koida, H. Sai, M. Kondo, *Thin Solid Films* 518/11, p. 2930.
- [13] H. Okamoto, Y. Nitta, T. Adachi, Y. Hamakawa, *Surface Science* 86 (1979), p. 486.
- [14] H. Matsuura, T. Okuno, H. Okushi, K. Tanaka, *Journal of Applied Physics* 55 (1984), p. 1012.
- [15] J. Kim, A. Abou-Kandil, K. Fogel, H. Hovel, D.K. Sadana, *ACS nano* 4/12 (2010), p. 7331.
- [16] Y. Park, V. Choong, Y. Gao, B. Hsieh, C. Tang, *Applied Physics Letters* 68 (1996), p. 2699.
- [17] T. Minami, T. Miyata, T. Yamamoto, *Surface and Coatings Technology* 108 (1998), p. 583.
- [18] A. Klein, *Applied Physics Letters* 77 (2000), p. 2009.
- [19] O. Lang, C. Pettenkofer, J. Sánchez-Royo, A. Segura, A. Kleina, W. Jaegermann, *Journal of Applied Physics* 86/10 (1999), p. 5687.
- [20] Y. Gassenbauer, A. Klein, *The Journal of Physical Chemistry B* 110/10 (2006), p. 4793.
- [21] K. Sugiyama, H. Ishii, Y. Ouchi, K. Seki, *Journal of Applied Physics* 87 (2000), p. 295.
- [22] K.H. Lee, H.W. Jang, K.B. Kim, Y.H. Tak, J.L. Lee, *Journal of Applied Physics* 95 (2004), p. 586.
- [23] M. Mason, L. Hung, C. Tang, S. Lee, K. Wong, M. Wang, *Journal of Applied Physics* 86 (1999), p. 1688.
- [24] F. Sánchez Sinencio, R. Williams, *Journal of Applied Physics* 54 (1983), p. 2757.
- [25] R. Rizzoli, R. Galloni, C. Summinte, R. Ringhini, E. Centurioni, F. Zignani, A. Desalvo, P. Ravy, A. Madan, *MRS Spring meeting*, San Francisco, 1997, p. 807.
- [26] Y. Tawada, M. Kondo, H. Okamoto, Y. Hamakawa, *Solar energy materials* 6/3 (1982), p. 299.
- [27] P. Sihanugrist, T. Sasaki, A. Asano, Y. Ichikawa, H. Sakai, *Solar Energy Materials and Solar Cells* 34/1-4 (1994), p. 415.
- [28] B.B. Van Aken, K.J. Bakker, M.C.R. Heijna, D. Reid, I. Baikie, W.J. Soppe, *physica status solidi (a)* 207/3, p. 682.
- [29] T. Söderström, F.J. Haug, V. Terrazzoni-Daudrix, C. Ballif, *Journal of Applied Physics* 103/11 (2008), p. 114509.
- [30] P. Pernet, M. Goetz, H. Keppner, A. Shah, *MRS Spring Meeting San Francisco*, 1996, p. 889.
- [31] K. Kuwano, S. Ashok, *Applied Surface Science* 117 (1997), p. 629.

- [32] E. Burstein, *Physical Review* 93/3 (1954), p. 632.
- [33] T. Moss, *Proceedings of the Physical Society. Section B* 67 (1954), p. 775.
- [34] A.P. Roth, J.B. Webb, D.F. Williams, *Physical Review B* 25/12 (1982), p. 7836.
- [35] T. Minami, H. Nanto, S. Takata, *Japanese Journal of Applied Physics* 24/8 (1985), p. L605.
- [36] I. Hamberg, C. Granqvist, K.F. Berggren, B. Sernelius, L. Engström, *Physical Review B* 30/6 (1984), p. 3240.
- [37] B. Pieters, J. Krc, M. Zeman, 4th World PVSEC, IEEE, Hawaii, 2007, p. 1513.
- [38] I. Ohdomari, K. Tu, *Journal of Applied Physics* 51/7 (1980), p. 3735.
- [39] M. Kubon, E. Boehmer, M. Gastel, F. Siebke, W. Beyer, C. Beneking, H. Wagner, IEEE, 1994, p. 500.
- [40] K. Ellmer, R. Mientus, *Thin Solid Films* 516/17 (2008), p. 5829.
- [41] T. Minami, H. Sonohara, T. Kakumu, S. Takata, *Thin Solid Films* 270/1-2 (1995), p. 37.
- [42] K. Ellmer, T. Welzel, MRS Spring Meeting, MRS, San Francisco, 2011.

**Table 1: Input parameters for electrical modelling. Schottky junctions with different barrier heights were assumed between ITO and the p2-layer.**

	<n>	<i>	<p1>	<p2>
Electron affinity (eV)	3.9	3.9	3.9	4.1
Band gap (eV)	1.85	1.85	1.9	1.15
Activation energy (eV)	0.3	(mid gap)	0.4	0.05
<i>(resulting work function)</i>	4.2	-	5.4	5.2
CB tail (eV)	0.6	0.04	0.05	-
VB tail (eV)	0.09	0.058	0.06	-

## Figure captions

Figure 1: Schematic cross section of an n-i-p solar cell.

Figure 2: Schematic band diagram of the ideal p-i-n junction (upper panel). The lower panels illustrate the formation of a Schottky barrier between the p-layer and the ITO front contact. Diagram b) illustrates the space charge region (SCR) of a partially depleted thick p-layer, diagram c) shows the situation of a realistic cell with thin p-layer; the i-layer is connected to the curved part of the completely depleted p-layer, thereby reducing the attainable built in voltage.

Figure 3: Work function variation of TCO films with respect to oxygen in the sputtering plasma, measured directly after deposition (deposition at 0.3 Pa, ECN setup).

Figure 4: Dependence of the open circuit voltage on the work function of the front ITO for 10 nm thick p1/p2 combinations of amorphous (p1) and microcrystalline (p2) p-layers. The inset illustrates the band alignment of the front contact layers for a fully amorphous p-layer (full lines) and for the 5/5 case (dashed lines), using an ITO work function of 5.1 eV.

Figure 5: Dependence of the resistivity on the oxygen content in the sputter plasma (deposition at 0.5 Pa, EPFL setup). Full and open symbols represent samples before and after annealing, respectively.

Figure 6: Variation of carrier density (upper panels) and Hall mobility (lower panels) with respect to the oxygen content in the sputtering plasma (deposition at 0.5 Pa, EPFL setup). Full and open symbols represent samples before and after annealing, respectively.

Figure 7: Dependence of the mobility on the carrier density for the different series of samples shown in Figure 6. Full and open symbols represent samples before and after annealing, respectively. The solid lines represent the limiting behaviour of ionized impurity scattering (Brooks, Herring, Dingle; BHD), the dashed line takes additionally into account the influence of grain boundary scattering [40].

Figure 8: Absorption of 60 nm thick ITO films on glass with respect to the oxygen content in the sputtering plasma. The shown films are sputtered from the 95/5 target, the other target compositions show similar behaviour. Full and dashed lines represent films before and after annealing, respectively.

Figure 9: Voc variation with respect to oxygen in the sputtering plasma during ITO deposition. For each target composition, the Voc of several cells on the same substrate is shown.

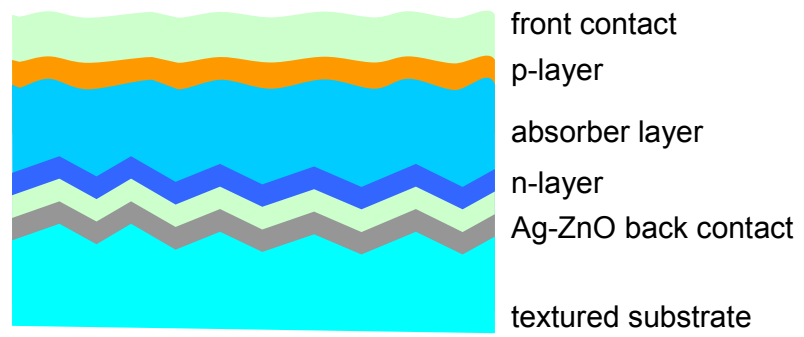


Figure 1: Schematic cross section of an n-i-p solar cell.

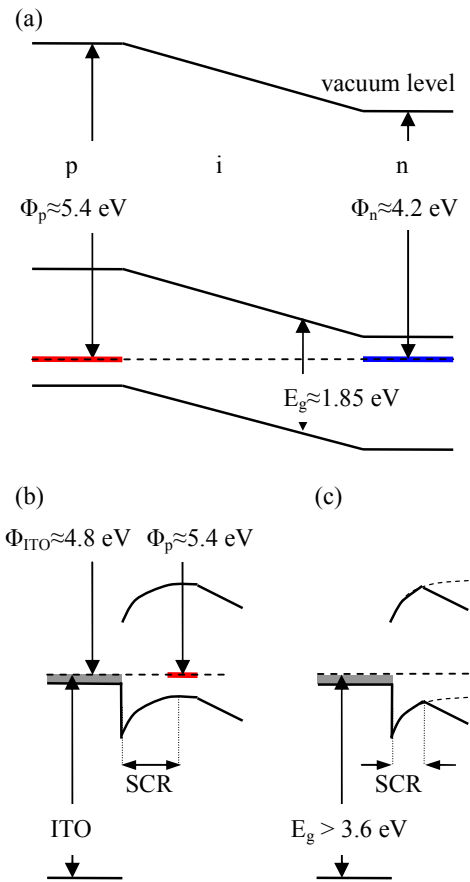


Figure 2: Schematic band diagram of the ideal p-i-n junction (upper panel). The lower panels illustrate the formation of a Schottky barrier between the p-layer and the ITO front contact. Diagram b) illustrates the space charge region (SCR) of a partially depleted thick p-layer, diagram c) shows the situation of a realistic cell with thin p-layer; the i-layer is connected to the curved part of the completely depleted p-layer, thereby reducing the attainable built in voltage.

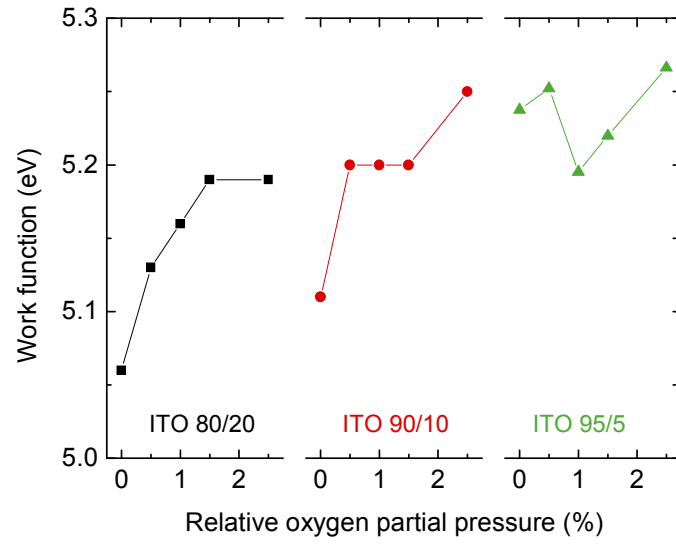


Figure 3: Work function variation of TCO films with respect to oxygen in the sputtering plasma

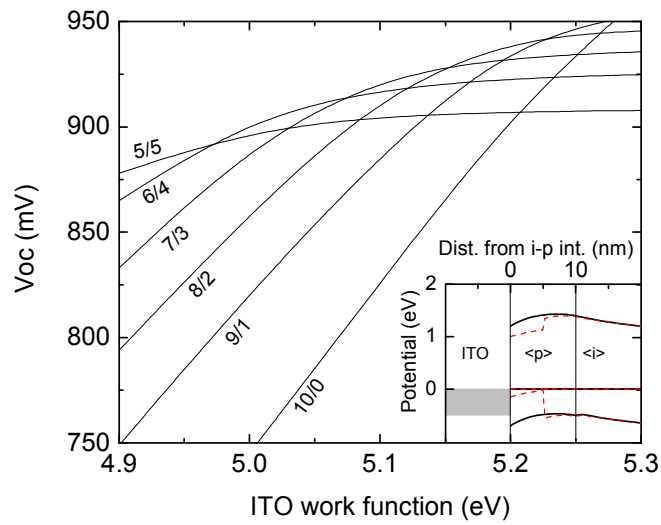


Figure 4: Dependence of the open circuit voltage on the work function of the front ITO for 10 nm thick p1/p2 combinations of amorphous (p1) and microcrystalline (p2) p-layers. The inset illustrates the band alignment of the front contact layers for a fully amorphous p-layer (full lines) and for the 5/5 case (dashed lines), using an ITO work function of 5.1 eV.

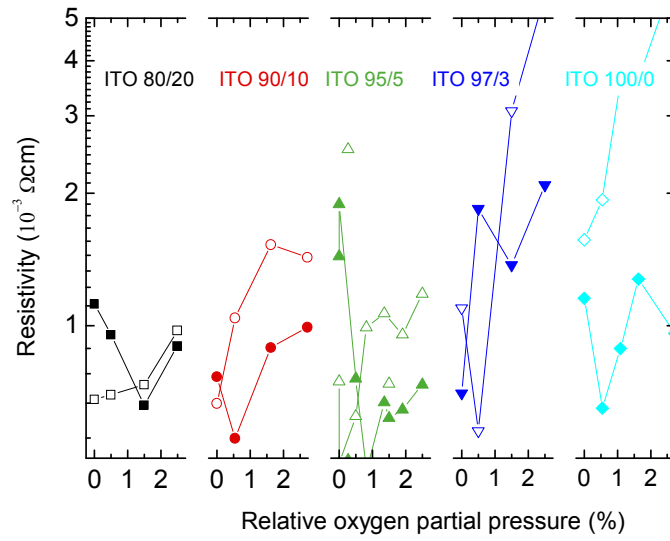


Figure 5: Dependence of the resistivity on the oxygen content in the sputter plasma (deposition at 0.5 Pa, EPFL setup). Full and open symbols represent samples before and after annealing, respectively.

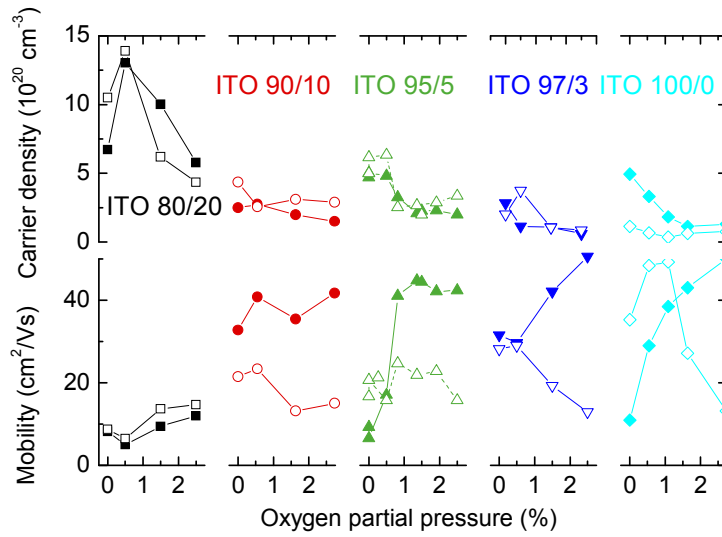


Figure 6: Variation of carrier density (upper panels) and Hall mobility (lower panels) with respect to the oxygen content in the sputtering plasma (deposition at 0.5 Pa, EPFL setup). Full and open symbols represent samples before and after annealing, respectively.

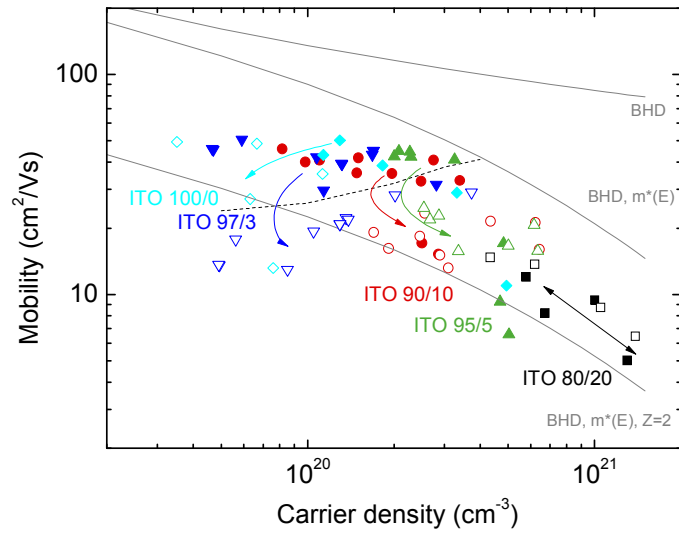


Figure 7: Dependence of the mobility on the carrier density for the different series of samples shown in Figure 6. Full and open symbols represent samples before and after annealing, respectively. The solid lines represent the limiting behaviour of ionized impurity scattering (Brooks, Herring, Dingle; BHD), the dashed line takes additionally into account the influence of grain boundary scattering [40].

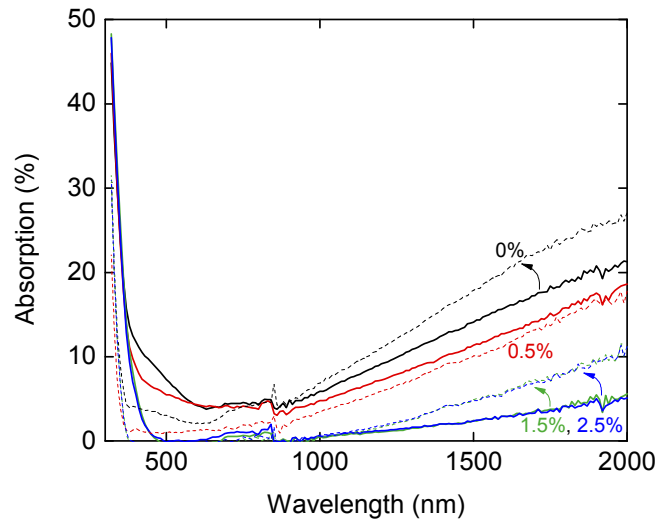


Figure 8: Absorption of 60 nm thick ITO films on glass with respect to the oxygen content in the sputtering plasma. The shown films are sputtered from the 95/5 target, the other target compositions show similar behaviour. Full and dashed lines represent films before and after annealing, respectively.

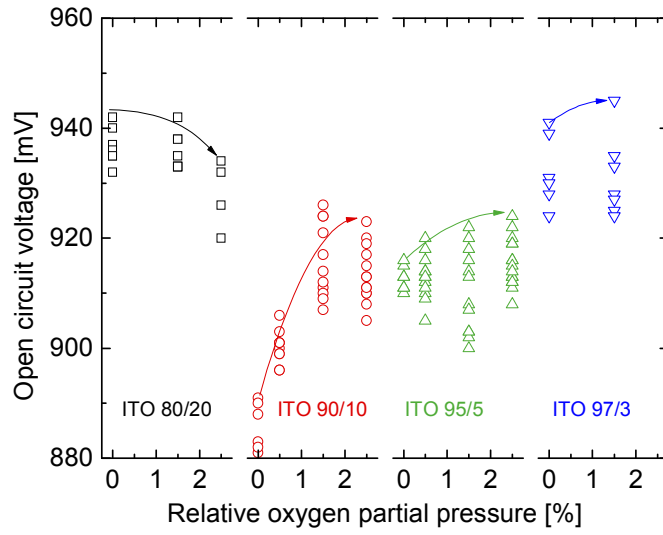


Figure 9: Voc variation with respect to oxygen in the sputtering plasma during ITO deposition. For each target composition, the Voc of several cells on the same substrate is shown.